Nanoscale

PAPER

Inserting ultrafine NiO nanoparticles into amorphous NiP sheets by in-situ phase reconstruction for high-stability of the HER catalysts

Chaoyang Sun[1], Hui Wang,[1,2] Jianwei Ren[3*], Xuyun Wang,[1] Rongfang Wang[1*]

P-based electrode electrocatalysts have exhibited high activities for hydrogen evolution reaction (HER), but their structural stabilities in the long-term operation of water electrolysis posed a technical challenge for the industrial-scale applications. In this study, amorphous NiP sheet arrays with rich active sites were created on the nickel foam (NF) by in-situ phase reconstruction, and then NiO ultrafine particles were generated within NiP sheets. The array electrode exhibited not only the enhanced catalytic activity verified by 76 mV of HER for NiO@NiP/NF at 10 mA cm^{-2}, but also the excellent structural stability in 1 M KOH solution proved by that the structure of the assembled electrode remained intact after 120 h long-term operation at 100 mA cm^{-2}

1. Introduction

Currently, water electrolysis-based hydrogen production has been expected to break its technical barriers towards green hydrogen economy[1-3]. For industrial-scale hydrogen production, the availability of the high active and robust electrode remains as one of the critical barriers[4, 5]. Although Ni-based electrodes have been employed widely in this regard, their catalytic activities and structural stabilities in particular need to be further improved [6-8].

As reported, the enhancement of catalytic activity is more relevant to the structure of the electrode by design[9-11]. Generally, the self-supported electrode structures with more flexibility appeared to achieve better performance than powder-bonded ones. Other electrode structures such as wire, tube and sheet shapes could lead to higher performance by increasing the specific surface area[12, 13]. The number of active sites could be increased through the thickness control on the catalyst sheet, and creation of structural defects or various heterostructures [14]. Some of the earlier research work has proven the viability of such strategy[15, 16]. For instance, Wang et al.[17] tailored the hollow structure within NiCoP nanowire arrays via nanoscale Kirkendall diffusion, and the enhanced hydrogen evolution reaction (HER) performance was achieved resulting from the higher surface area and better permeability. Yu et al [14] engineered porous Ni$_2$P-nanoparticle and Ni$_2$P-nanosheet arrays through Kirkendall effect and Ostwald ripening. The obtained electrocatalyst with rich homogeneous grain boundaries improved the efficiency of the overall water splitting. In the work of Wang et

al.[6], the catalytic oxygen evolution reaction (OER) and HER performance were boosted by integrating Ni nanoparticles into MoN nanosheets from Schottky heterojunctions. However, in their experiments, the long-term stability of the catalysts encountered a problem, which was attributed to the reduction of heterostructures after the grain boundaries were restructured into amorphous phases [18]. Similar results were also reported by other research groups, for example, Sun et al.[19] anchored porous Ni microspheres into nickel foam via a template-free electrodeposition, and the phosphidation process was further employed to yield Ni$_2$P/Ni/NF catalysts with 3D configuration. Such hierarchically macroporous structures were found to reduce ion transport resistance and facilitate the diffusion of gaseous products (H$_2$ and O$_2$). During the stability tests for oxygen evolution reaction (OER), the cell voltages fluctuated because partial Ni$_2$P/Ni/NF catalyst was oxidized to nickel oxides and hydroxides on the catalyst surface [20, 21].

These earlier works indicated that the electrode structure can be tuned by in-situ phase reconstruction to increase the number of the active sites within the catalysts, so as that higher catalytic performance could be achieved [22-24]. In this work, the previously synthesized Ni$_2$P nanosheet arrays were converted to amorphous phase by in-situ phase reconstruction [25]. Meanwhile, some of the metallic Ni were oxidized to ultrafine NiO particles and embedded into Ni$_2$P nanosheet arrays. The number of the active sites were increased significantly resulting from both homogenous and heterogeneous grain boundaries formed by amorphous NiP nanosheet arrays and NiO/NiP interface. Eventually, the prepared electrode showed the enhanced HER catalytic performance and long-term cycling stability [25].

2、Experimental Section

2.1 Preparation of Ni$_2$P/NF sample

The surface oxide layer of the nickel foam (2×3 cm^2) was removed by firstly putting the sample into 20 mL 1.0 M HCl solution

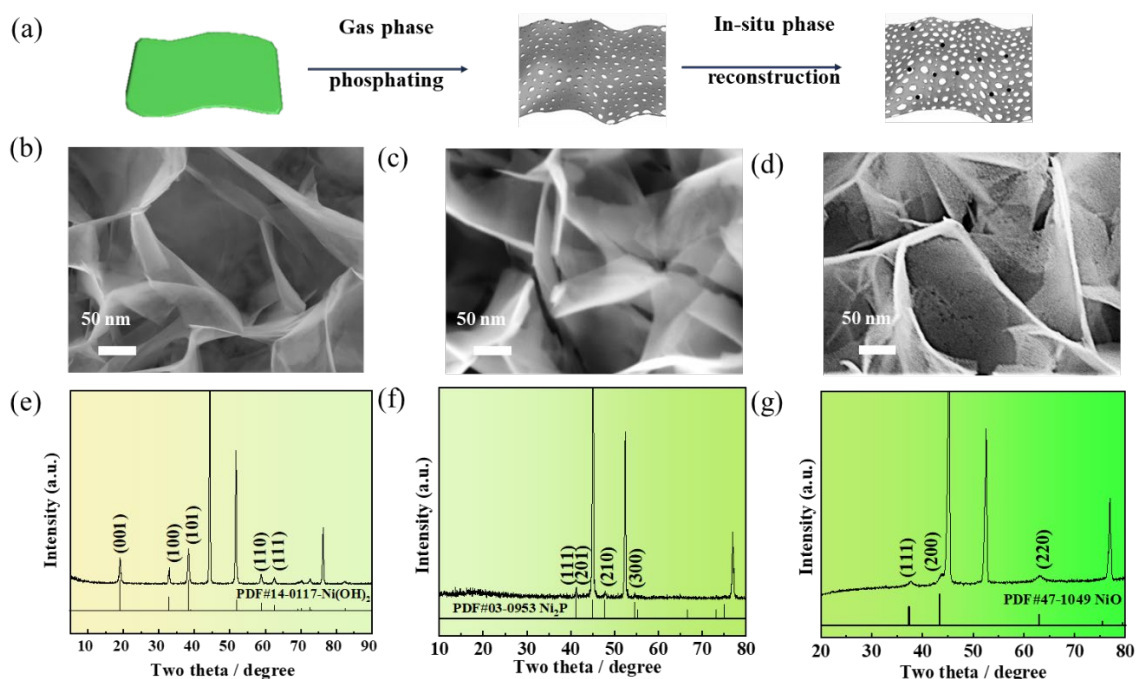to ensure that it was completely immersed and subsequently ethanol solution

Figure 1. (a) Schematic formation of NiO@NiP/NF, SEM images and XRD patterns of Ni(OH)$_2$/NF(b,e), Ni$_2$P/NF (c,f), and NiO@NiP/NF(d,g).

for 15 min under ultrasound. Then, the pre-treated nickel foam was washed using water and dried at 60 ℃ under vacuum. After that, the dry nickel foam was put into a 100 mL autoclave containing 20 mL $3.6×10^{-3}$ M HCl solution and kept at 100 ℃ for 20 h to obtain the Ni(OH)$_2$/NF sample. To derive the Ni$_2$P/NF sample, 0.03 g NaH$_2$PO$_2$ was located at the lower position of a tube furnace under N$_2$ flow, and the clean Ni(OH)$_2$/NF sample was treated in the upper position with at 350 ℃ for 2 h.

2.2 Preparation of NiO@NiP/NF sample

The in-situ phase reconstruction of Ni$_2$P/NF sample to NiO@NiP/NF was done in a three-electrode electrochemical cell, wherein Ni$_2$P/NF obtained from Section 2.1 was assembled as working electrode, graphite rod and Hg/HgO (1 M KOH) were used as counter electrode and reference electrode, respectively. The cyclic voltammetry (CV) experiments were carried out for 100 cycles at 0.2 ~ 0.6 V in 1 M KOH electrolyte.

3、Results and discussion

Figure 1a illustrates the typical procedure in which Ni(OH)$_2$/NF underwent static gas-phase phosphating, and in-situ electrochemical oxidation to obtain NiO@NiP/NF sample. It can be seen from scanning electron microscope (SEM) images in Figure 1b-d that after the Ni(OH)$_2$/NF sample went through phosphating process (Ni$_2$P/NF) and in-situ phase reconstruction

(NiO@NiP/NF), the intense nanosheet arrays with thickness of 10–20 nm were still well maintained, as clearly shown in Figure S1. It was noticed that the surface of NiO@NiP/NF became porous, which was attributed to the P-leaching as well as the formation of NiO during CV cycles. The porous surface structure would provide not only more active sites for water electrolysis but also the channel for mass transfer.

The X-ray diffraction (XRD) pattern in Figure 1f exhibits several diffraction peaks positioned at 40.8°, 44.6°, 47.3° and 54.9° corresponding to the (111), (201), (210) and (300) planes of Ni$_2$P/NF (JCPDS#03-0953), respectively, which suggests that Ni$_2$P/NF structure has been successfully prepared. Similarly, the formation of NiO@NiP/NF structure can be evidenced by the XRD signals in Figure 1g, wherein peaks at 37.2°, 43.2° and 62.8° agree well with the (111), (200) and (220) planes of NiO (JCPDS#47-1049), respectively. Furthermore, the CV peak of NiO in Figure S2 shifted to the higher potential, indicating the metallic Ni was oxidized to a higher valence. Meanwhile, the absence of Ni$_2$P diffraction peaks in Figure 1g implies the transition of Ni$_2$P to NiO and amorphous phase. It is well accepted that nickel phosphides generally convert to corresponding hydroxides or oxyhydroxides under electrocatalytic conditions for OER. Here, the absence of the Ni(OH)$_2$
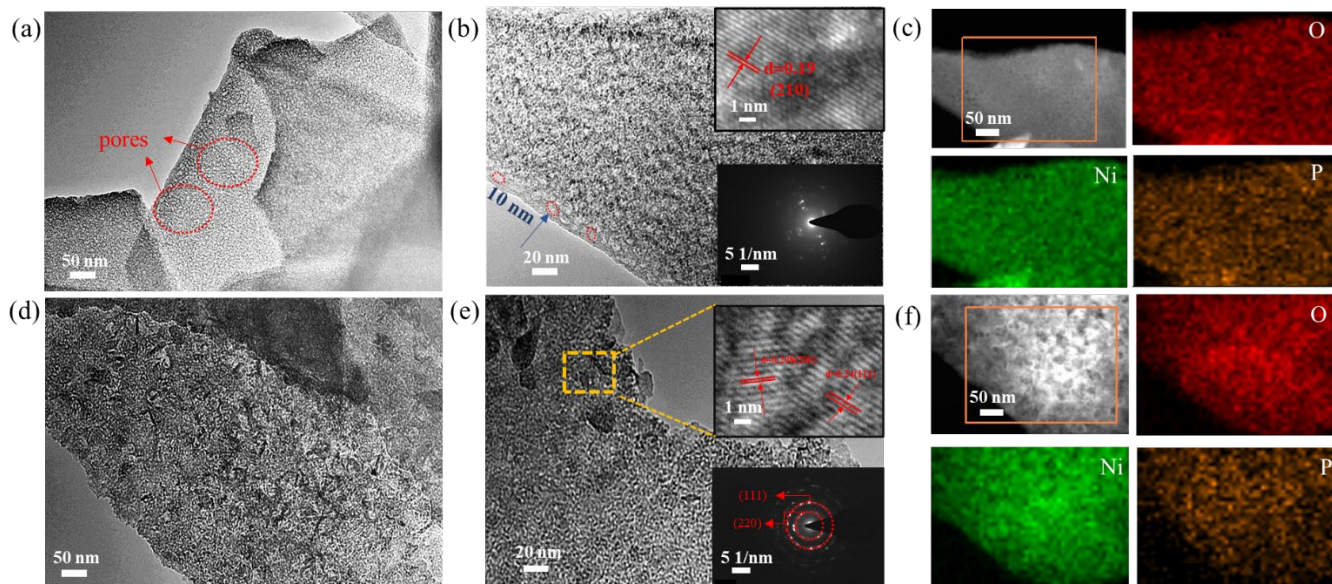
Nanoscale

Figure 2. (a-b) TEM and HR-TEM images of Ni$_2$P/NF. (c) STEM and elemental mappings of Ni, P, O elements of Ni$_2$P/NF. (d-e) TEM and HR-TEM images of NiO@NiP/NF. (f) STEM and elemental mappings of Ni, P, O elements of NiO@NiP/NF.

or NiOOH XRD diffraction peaks suggests the absence of their crystalline particles, but there is possibility for the presence of amorphous Ni(OH)$_2$ or NiOOH.

To further understand the process of phase reconstruction, Figure 2(a-c) show the transmission electron microscope (TEM) and high-resolution TEM (HRTEM) images of Ni$_2$P/NF sample. The porous surface structure with pore size around 10 nm can be clearly observed, and there are Ni$_2$P nanoparticles embedding within the nanosheets, which was confirmed by the earlier XRD tests. The interplant distance of 0.19 nm in the inset image of Figure b belongs to the (210) plane of Ni$_2$P. The elemental mappings in Figure c shows the well-distributed Ni, P and O elements within the Ni$_2$P/NF sample. The TEM and HR-TEM images of NiO@NiP/NF sample are shown in Figure 2(d-e). The change of the surface morphology and the reduction of dark dots reveal the phase reconstruction during CV cycles and P-leaching. The lattice fringes of 0.24 nm and 0.208 nm appeared in the insert image of Figure 2e can be assigned to the (111) and (220) planes of NiO, respectively. The elemental mapping in Figure 2f reveals the existence of P elements. This suggests that while samples were CV scanned at high potential of 0.2 ~ 0.6 V, P elements were oxidized, migrated to the surface of the sample, and even dissolved in the electrolyte, resulting in an irreversible process. In the further oxidation process, P was substituted by O and combined with Ni to form NiO. Under well controlled reaction conditions, the Ni elements were only partially oxidized to NiO. From elemental mapping images, it was found that P element was still uniformly distributed in the sample, but there was no obvious XRD diffraction peak observed. This implies that the sample was re-structured into amorphous Ni-P phase in this process.

In our experiments, the porous surface structure of Ni$_2$P nanosheet arrays was obtained from an optimal process. As shown in Figure S3, in the CV process for phase-reconstruction, the crystallinity of NiO increased with the increasing CV cycles. This indicates that more and more NiO crystalline were formed. Meanwhile, the increasing intensity of the NiO XRD diffraction peaks suggests that the NiO particles are getting bigger. From the comparison of CV curves in Figure S4(a), the oxidation and reduction peaks of Ni$_2$P/NF sample appear at 0.47 V and 0.32V in the 1st cycle at 0.2~0.6 V. This clearly increased current response on the NiO@NiP/NF electrode indicates more exposed active sites. The oxidation peak for NiO@NiP/NF shifts to the higher potential after 100 cycles compared to that of Ni$_2$P/NF, suggesting that NiO@NiP/NF sample was obtained with the co-existence of Ni^{2+} and Ni^{3+} on the surface. The linear sweep voltammogram (LSV) curves in Figure S4 (b) implies the improved catalytic activities after various cycles of oxidation, and Figure S4 (c) suggests the optimal electrochemical oxidation is 100 cycles. In other words, the NiO/NiP grain boundaries at this point of time were created readily to be the active sites with enhanced catalytic activities. Besides, the tests on electrical

conductivities in Figure S4 (d) shows a value of 0.0797 KS/mm for NiO@NiP/NF sample, which is lower than that of Ni$_2$P/NF sample
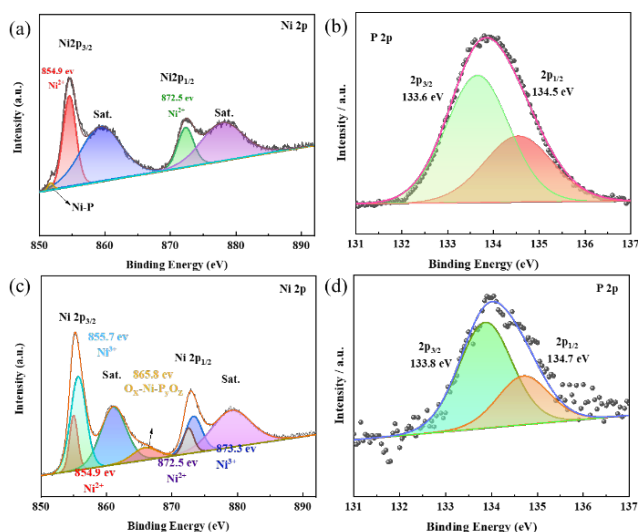

Figure 3. The deconvoluted high-resolution Ni 2p and P 2p XPS spectra of Ni$_2$P/NF(a,b) and NiO@NiP/NF(c,d).

(0.0815 KS/mm). Such change was caused by the formation of NiO compound with the lower conductivity compared to Ni$_2$P. This agrees with literature that the electrical conductivities will drop after oxidation because of the coverage of oxide layers on the sample surfaces [26].

Later on, X-way photoelectron spectra (XPS) tests were conducted to further probe the change of surface compositions. Figure 3a shows the deconvoluted XPS spectra of Ni 2p within Ni$_2$P/NF sample. The peak at 851.7 eV belongs to Ni-P bond. Two peaks at 854.9 eV and 872.5 eV are assigned to the oxided Ni^{2+}, and the other two peaks at 861.1 eV and 879.1 eV correspond to satellite peaks.[27,28] Those observations agree very well with the XRD testing results. For the deconvoluted XPS spectra of Ni 2p within NiO@NiP/NF sample (Figure 3c), the two peaks at 854.9 eV and 872.5 eV can be assigned to oxided Ni^{2+}, and the other two peaks at 855.7 eV and 873.3 eV belong to oxided Ni^{3+}.[27,28] The extra peak appearing at 865.8 eV is ascribed to O$_x$-Ni-P$_y$O$_z$.[29] These evidences confirmed the appearance of new phases after 100 CV cycles, and Ni^{3+} plays an important role for the enhanced catalytic activities. The co-existence of Ni-O and Ni-P offered the electrode with more active sites and better electrical conductivity, which facilitated the transfer of electrons in catalysis processes.

Figure 3b and 3d show the deconvoluted XPS spectra of P, 2p. Overall, the lower intensity of P element in NiO@NiP/NF sample suggests a lower P content compared to that in Ni$_2$P/NF sample. This reduction was caused by the oxidation and leaching of P during CV process, as confirmed by values in Table

S1. Both P 2P peaks from two samples are situated at around 134ev, and this implies their oxidation states resulting from the contacting with air[30]. As observed in Figure 3b and 3d, the two 2P1/2 and 2P3/2 peaks in NiO@NiP/NF sample shifted towards the positive direction by 0.3 eV compared to that of Ni$_2$P/NF sample, which suggests a weaker shielding effect around P element. This is caused by the participation of O atom in NiO@NiP/NF sample with much stronger electronegativity than that of P atom. This is to say, the formation of NiO crystalline in NiO@NiP/NF sample led to the electron structural change of NiP compound, which in turn will affect the hydrogen adsorption/desorption behaviors and eventually impact the catalytic performance.

The HER catalytic performance was evaluated through linear sweep voltammetry (LSV) in 1.0 M KOH electrolyte at a scan rate of 5 mV s^{-1}. It can be seen from Figure 4a-b that NiO@NiP/NF sample exhibited the low onset potential of HER, and overpotential with 76 mV and 142 mV at 10 mA cm^{-2} and 50 mA cm^{-2}, respectively. Although such performance is still lower than that of Pt/C/NF catalyst, it enhanced by 77 mV compared to that of Ni$_2$P/NF sample. As shown in Figure 4c, the calculated Tafel slopes of NiO@NiP/NF and Pt/C/NF sample are 98 mV dec^{-1} and 69 mV dec^{-1}, respectively. As understood, the lower value of Tafel slope represents the faster HER kinetics[31].

The electrochemical impedance spectroscopy (EIS) spectra were measured to get further understanding on the good catalytic activity of the NiO@NiP/NF. As shown in Figure 4d, NiO@NiP/NF sample exhibits a low liquid junction resistance of 1.5 Ω because the porous nanosheet structure is favorable for the wettability. The low charge transfer resistance of 5.8 Ω resulted from the excellent electrical conductivity and higher electrode dynamics of NiP[32]. For the HER catalyst, the effective electrochemical active surface evaluated based on the electrochemical double-layer capacitance was always to further reveal the origin of their activity. Here, the as-prepared samples were tested by the CV curves in the non-Faradaic potential region at different scan rates, as presented in Figure S5. Then, the plots related scan rates to J_a-J_c at 0.21 V (vs. RHE) in Figure 4e was obtained, from which the active surface area of NiO@NiP/NF increased from Ni$_2$P/NF sample, which can result from the porous structure, rich grain boundaries and amorphous phase.

As displayed in Figure 4f, the Chronopotentiometric (CP) tests conducted at a current density of 100 mA cm^{-2} for 120 h showed a nearly unchanged potential throughout time, suggesting the high stability of NiO@NiP/NF electrode. Most notably, compared to the reported NiP-based
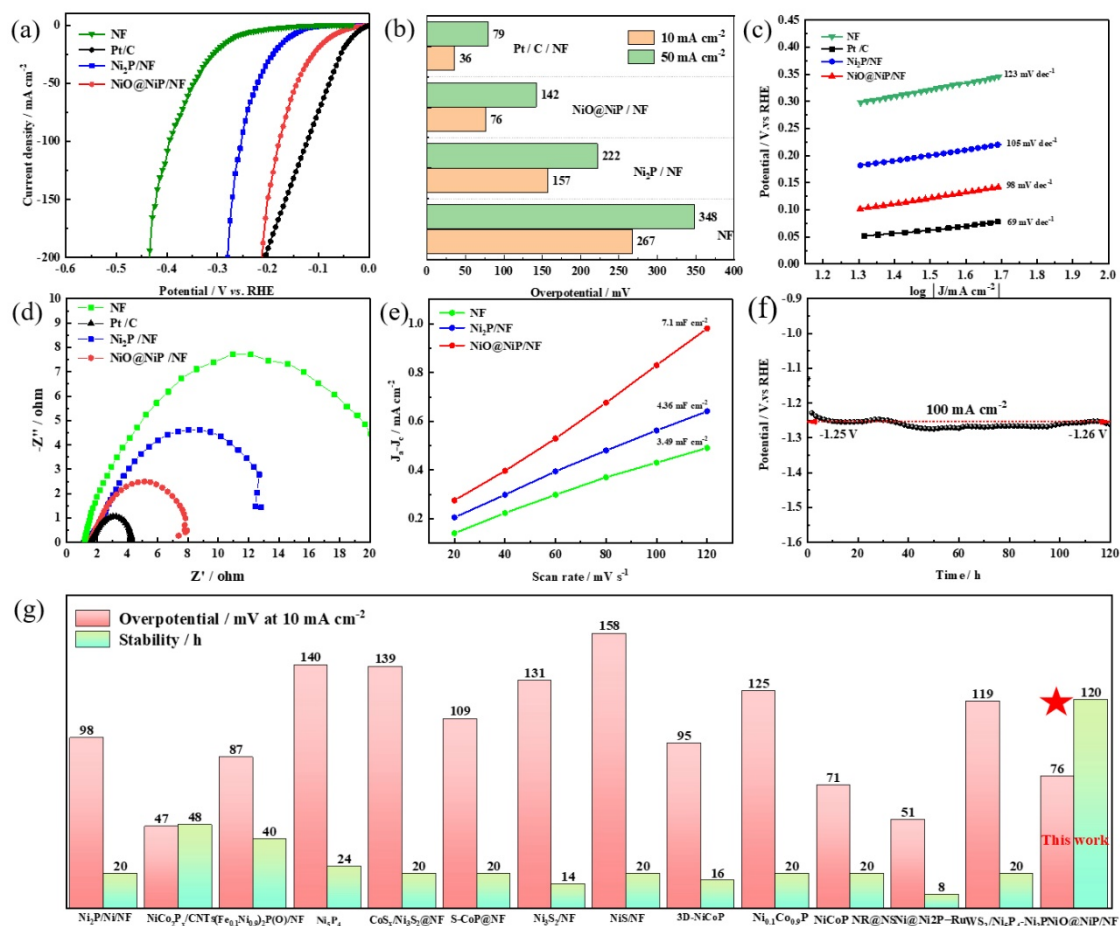
Nanoscale

Figure 4. (a) HER LSVs in 1.0 M KOH at a scan rate of 5 mV s^{-1}; (b) corresponding overpotential at 10 mA cm^{-2} and 50 mA cm^{-2} respectively; (c) their Tafel plots; (d) EIS spectra of Pt/C/NF, Ni$_2$P/NF, NiO@NiP/NF electrodes; (e) linear fitting of HER $\triangle$j *vs.* scan rates at +0.216 V *vs.* RHE of NF, Ni$_2$P/NF, NiO@NiP/NF electrodes; (f) the CP curves tested for 120 h at a current density of 100 mA cm^{-2} of NiO@NiP/NF electrode; and (g) Comparison of the electrode performance between NiO@NiP/NF and other electrodes reported in the literature.

electrodes listed in Figure 4g, the NiO@NiP/NF possesses excellent stability for HER. The structure of the NiO@NiP/NF after long-term tests was characterized to reveal the origin of its stability. As revealed by the SEM images in Figure 5a-c, the array configuration assembled of the thin sheets retained after long-term catalysis. XRD pattern of the NiO@NiP/NF after the 120 h CP test shows the diffraction peaks of NiO and is still short of the characteristic peaks of Ni$_2$P (Figure S6), which is same to that before the CP test, proving the phase of the NiO@NiP/NF did not change. Meanwhile, the fine structure of the sheet primitive, thin and porous property, is retained judging from the

TEM images in Figure 5d-f. The lattice fringe corresponding to the (200) plane of NiO can still be observed from the HRTEM image in Figure 5f, agrees with the XRD observation. The above results indicate the good stability of the NiO@NiP/NF is attributed to its unique structure formed by in-situ phase reconstruction.

4. Conclusion

In summary, the in-situ phase reconstruction was achieved in this study after P-leaching to derive NiO@NiP/NF material with enhanced HER catalytic performance. The formation of NiO ultrafine particles within amorphous NiP nanosheets increased the number of active

sites for HER, and the excellent electrical conductivity of NiP nanosheets further improved the electrode dynamics. This approach provided a promising solution toward the technical issues such as the instability of Ni_2P and poor electrical conductivity of NiO. As a result,

the assembled electrode exhibited HER overpotential of 76 mV at 10 mA cm^{-2}, and good structural stability in 1 M KOH solution after 120 h long-term operation.
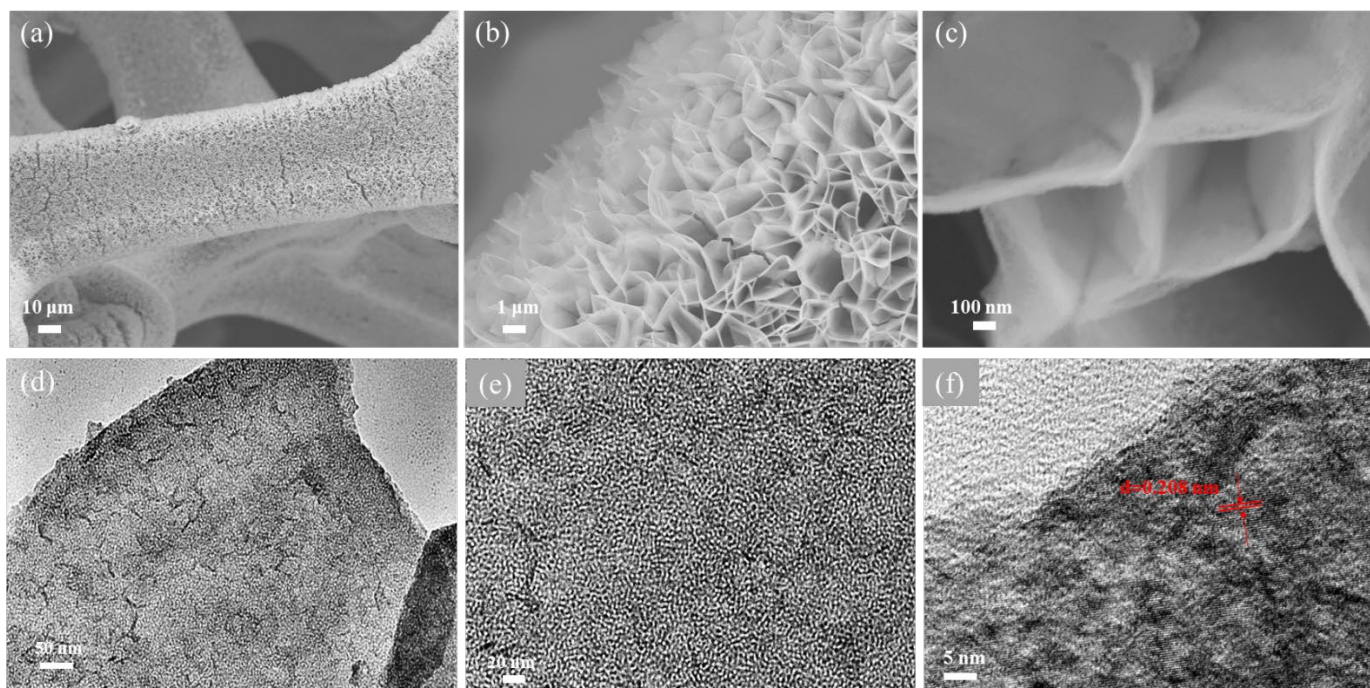

Figure 5. (a-d) SEM images of NiO@NiP/NF at different magnification after stability test. (e-f) TEM and HR-TEM images of NiO@NiP/NF at different magnification after stability test.

Conflicts of interest

There are no conflicts to declare.

Notes and references

1. W. Chen, H. Wang, Y. Li, Y. Liu, J. Sun, S. Lee, J. S. Lee and Y. Cui, *ACS Cent Sci*, 2015, **1**, 244-251.

2. S. Anantharaj and S. Noda, *Small*, 2020, **16**, 1905779.

3. W. Zhan, L. Sun and X. Han, *Nanomicro Lett*, 2019, **11**, 1.

4. J. Xiao, L. Wan, S. Yang, F. Xiao and S. Wang, *Nano Letters*, 2014, **14**, 831-838.

5. S. Shit, S. Chhetri, W. Jang, N. C. Murmu, H. Koo, P. Samanta and T. Kuila, *ACS Appl Mater Inter* 2018, **10**, 27712-27722.

6. Z. Wang, J. Lu, S. Ji, H. Wang, X. Wang, B. G. Pollet and R. Wang, *J. Alloys Compd*, 2021, **867**,158983

7. Z. Tan, L. Sharma, R. Kakkar, T. Meng, Y. Jiang and M. Cao, *Inorg. Chem*, 2019, **58**, 7615-7627.

8. L. Zhang, H. Wang, S. Ji, X. Wang and R. Wang, *Dalton Trans*, 2019, **48**, 17364-17370.

9. L. Su, X. Cui, T. He, L. Zeng, H. Tian, Y. Song, K. Qi and B. Y. Xia, *Chem. Sci*, 2019, **10**, 2019-2024.

10. A. Sivanantham, P. Ganesan, A. Vinu and S. Shanmugam, *ACS Catal*, 2019, **10**, 463-493.

11. F. Polo-Garzon, Z. Bao, X. Zhang, W. Huang and Z. Wu, *ACS Catal*, 2019, **9**, 5692-5707.

12. M. Miao, R. Hou, R. Qi, Y. Yan, L. Q. Gong, K. Qi, H. Liu and B. Y. Xia, *J. Mater. Chem. A*, 2019, **7**, 18925-18931.

13. P. W. Menezes, C. Panda, C. Walter, M. Schwarze and M. Driess, *Adv. Funct. Mater*, 2019, **29**, 1808632.

14. Y. Wu, H. Wang, S. Ji, B. G. Pollet, X. Wang and R. Wang, *Nano Res*, 2020, **13**, 2098-2105.

15. Y. Li, X. Du, J. Huang, C. Wu, Y. Sun, G. Zou, C. Yang and J. Xiong, *Small*, 2019, **15**, 1901980.

16. N. Cheng, Q. Liu, A. M. Asiri, W. Xing and X. Sun, *J. Mater. Chem. A*, 2015, **3**, 23207-23212.

17. H. Wang, X. Shi, S. Ji, X. Wang, L. Zhang, H. Liang, D. J. L. Brett, X. Wang and R. Wang, *Nanotechnology*, 2020, **31**, 425404.

18. M. A. R. Anjum, M. S. Okyay, M. Kim, M. H. Lee, N. Park and J. S. Lee, *Nano Energy*, 2018, **53**, 286-295.

19. B. You, N. Jiang, M. Sheng, M. W. Bhushan and Y. Sun, *ACS Catal*, 2015, **6**, 714-721.

20. M. Favaro, C. Valero-Vidal, J. Eichhorn, F. M. Toma, P. N. Ross, J. Yano, Z. Liu and E. J. Crumlin, *J. Mater. Chem. A*, 2017, **5**, 11634-11643.

21. W. L. Xiaoguang Wang, Dehua Xiong and Lifeng Liu, *J. Mater. Chem. A*, 2016 **4**, 5639-5646.

22. W. Sun, C. Ma, X. Tian, J. Liao, J. Yang, C. Ge and W. Huang, J. Mater. Chem. A, 2020, **8**, 12518-12525.

23. Q. Wang and K. Domen, *Chem Rev*, 2020, **120**, 919-985.

24. Z. Wang, H. Wang, S. Ji, X. Wang, B. G. Pollet and R. Wang, *J. Power Sources*, 2020, **446**, 227348.

25. G. Ren, Q. Hao, J. Mao, L. Liang, H. Liu, C. Liu and J. Zhang, *Nanoscale*, 2018, **10**, 17347-17353.

26. I. C. Man, H. Y. Su, F. Calle- Vallejo, H. A. Hansen, J. I. Martínez, N. G. Inoglu, J. Kitchin, T. F. Jaramillo, J. K. Nørskov and J. Rossmeisl, *ChemCatChem*, 2011, **3**, 1159-1165.

27. X. Shi, J. Key, S. Ji, V. Linkov, F. Liu, H. Wang, H. Gai, R. Wang, Small, 2018, **15**, 1802861.

28. X. Shi, H. Wang, P. Kannan, J. Ding, S. Ji, F. Liu, H. Gai, and R. Wang, J. Mater. Chem. A, 2019, **7**, 3344-3352

29. S. H. Yu, W. Chen, H. Wang, H. Pan and D. H. C. Chua, *Nano Energy*, 2019, **55**, 193-202.

30. M. Ledendecker, S. Krick Calderon, C. Papp, H. P. Steinruck, M. Antonietti and M. Shalom, *Angew Chem Int Ed Engl*, 2015, **54**, 12361-12365.

31. J. Lu, C. Li, H. Wang, S. Ji, X. Wang and R. Wang, Int. J. Hydrog. Energy, 2021, **46**, 12936-12943.

32. X. Lv, S. Ji, V. Linkov, X. Wang, H. Wang and R. Wang, J. Mater. Chem. A, 2021, **9**, 2928-2936.